EES Solar

PAPER

View Article Online
View Journal

Cite this: DOI: 10.1039/d6el00044d

Interplay of diffusion and crystallization in sequentially evaporated lead tin perovskites

Lara M. van der Poll, [a] Moisés Cámara Díaz,[a] Reinder K. Boekhoff,[b] Poojalakshmi Vageeswaran,[c] Niels van Silfhout, [a] Luana Mazzarella, [b] Swapna Ganapathy, [d] Lars J. Bannenberg, [d] Dibyajyoti Ghosh,[c] Arno H. M. Smets[b] and Tom J. Savenije *[a]

Low bandgap (LBG) Pb–Sn perovskites (PVKs) are key absorber materials for high-efficiency all-perovskite tandem solar cells. Yet, their fabrication at device-relevant thicknesses with high structural and optoelectronic quality remains challenging. Here, we demonstrate the scalable deposition of formamidinium lead tin triiodide ($FAPb_{0.5}Sn_{0.5}I_3$) films up to 700 nm thick using a single cycle of sequential thermal evaporation (1c-sTE). The process relies on vacuum deposition of a $PbSnI_4$ alloy followed by FAI, without the need for additives typically used in solution processing. Optical spectroscopy, XRD, solid-state NMR, and TRMC measurements reveal that FAI readily diffuses into the inorganic precursor layer even at room temperature. Independent of the precursor mixing time, annealing is required to achieve films with increased local homogeneity, large grains, and high crystallinity, leading to reduced defect density, increased carrier mobility up to 80 cm^2 (Vs^{-1}), and lifetimes close to a microsecond. The resulting films are stoichiometrically uniform across their thickness and exhibit dense, columnar grain morphologies. A device with the architecture ITO/PEDOT:PSS/$FAPb_{0.5}Sn_{0.5}I_3$/C60/BCP/Ag, shows power conversion efficiencies of 10%, with voltage losses mainly at the PEDOT:PSS/PVK interface. This work demonstrates that 1c-sTE is a feasible method for producing LBG Pb–Sn PVK films suitable for PV applications.

Received 6th March 2026
Accepted 8th May 2026

DOI: 10.1039/d6el00044d

rsc.li/EESSolar

Broader context

As the world transitions toward sustainable energy, solar power is playing an increasingly important role, driven by its abundance, scalability, and position among the most cost-effective sources of electricity. However, meeting rising energy demand requires solar cells with efficiencies beyond the limits of conventional technologies. Metal halide perovskites have emerged as contenders, rivaling silicon in performance. Their electronic properties are tunable, enabling the design of multi-absorber solar cells. In this context, low bandgap perovskites are needed to harvest low-energy light, while reducing toxic lead content and developing scalable, industry-ready fabrication methods remain critical challenges. Here, we partially replace lead with tin to lower toxicity and achieve the desired bandgap. We deposit the films by thermal evaporation in vacuum. The precursors spontaneously mix after deposition, forming the desired perovskite phase. This enables the use of two precursor layers, whereas other lead-based perovskite compositions require multiple deposition cycles. However, post-deposition thermal annealing remains crucial to obtain highly crystalline, compositionally homogeneous films with low defect densities and excellent charge transport properties. Our findings advance understanding of the conversion in thermally evaporated low bandgap tin lead perovskites and demonstrate a viable and scalable route towards commercial perovskite solar cells.

Introduction

Metal halide perovskites (PVKs) have emerged as highly promising absorber layers in single-junction solar cells, resulting in efficiency records exceeding 27%.[1] Their integration into perovskite solar cells (PSCs) is facilitated by their desirable optoelectronic properties for photovoltaic (PV) applications, including tunable bandgaps, relatively high absorption coefficients, and defect tolerance.

A considerable amount of research on PSCs is devoted to combining PVKs with silicon or with PVKs of differing bandgaps to enhance the utilization of the solar spectrum and thereby maximize the power conversion efficiency (PCE).[2–5] All-PVK tandems require a combination of wide bandgap (WBG, ~1.7–1.8 eV) and low bandgap (LBG, ~1.2–1.3 eV) PVK absorber layers, which are engineered by modifying the composition of the characteristic ABX_3 structure. WBG perovskites are formed

[a]Department of Chemical Engineering, Delft University of Technology, The Netherlands. E-mail: t.j.savenije@tudelft.nl
[b]Department of Electrical Sustainable Energy, Delft University of Technology, The Netherlands
[c]Department of Materials Science and Engineering, Department of Chemistry, Indian Institute of Technology, New Delhi, India
[d]Reactor Institute Delft, Delft University of Technology, Delft, Netherlands

by partially substituting iodide (I^-) with bromide (Br^-) at the X-site, while LBG PVKs are achieved by replacing lead (Pb^{2+}) with tin (Sn^{2+}) at the B-site. The A-site, occupied by monovalent cations, such as methylammonium (MA^+), formamidinium (FA^+), and cesium (Cs^+), mainly stabilizes the crystal structure with minimal impact on the bandgap.

Today, PVK thin films are still mostly produced from solution. In this process, the precursors are dissolved in a common, often toxic, solvent and, at the lab scale, typically deposited by spincoating. Industrial PVK production from solution has been demonstrated using scalable techniques, such as slot-die coating, blade coating, and inkjet printing.[6–9] Yet, achieving high crystallinity and uniformity in large-area films remains challenging due to the complex dynamics during film formation. For LBG PVKs, various additives are used to mediate crystallization, suppress oxidation, and achieve the desired film phase and morphology. However, these additives can introduce new defects, leading to performance losses, and may also compromise device stability if not carefully optimized.[10–13]

Alternatively, PVK layers can be produced by physical vapor deposition in vacuum, *e.g.*, thermal evaporation (TE). This technique has garnered increased attention in recent years due to its scalability, adaptability, and ability to uniformly coat textured surfaces.[13–15] These traits make it a highly suitable method specifically to produce multi-layered device architectures. Two primary modes of TE are used: coevaporation (cTE) and sequential evaporation (sTE). In cTE, all precursors are deposited simultaneously, and compositional control is achieved by tuning the ratio of the individual precursor sublimation rates. cTE is enticing for industry due to the fast deposition speeds that are possible. However, achieving stoichiometric films is complex due to rate- and pressure-dependent interactions between the precursor streams.[16,17] Despite these challenges, cTE has repeatedly enabled the fabrication of 1-j PSCs with efficiencies beyond 20%.[18–20] Contrary to cTE, sTE involves the stepwise deposition of the separate precursors in a layer-by-layer approach. This method is comparatively simpler than cTE, offering improved control over the film stoichiometry and greater reproducibility, albeit with longer processing times. Like cTE, sTE has aided in the production of 1-j lead-based PSCs with a PCE of 24%.[21]

It has been shown that producing LBG PVKs in vacuum conditions yields high-quality thin films.[22–25] Notably, TE offers a significant advantage by inherently suppressing the oxidation of tin(II) to tin(IV) during processing. This reaction opens degradation pathways that severely inhibit cell performance and readily occur in the presence of oxygen, moisture, and other impurities. These factors are difficult to eliminate in a solvent-based process, and additives such as tin(II) fluoride (SnF_2) are frequently incorporated to mitigate the aftermath of tin(II) oxidation.[26–28] Focusing specifically on the TE of LBG perovskites, cTE has been successfully employed to fabricate single-junction PSCs with power conversion efficiencies of up to 14%. These efficiencies are relatively low compared to the state-of-the-art spincoated devices, which have achieved champion efficiencies of around 24%.[29] However, those devices have undergone extensive optimization over many years of research. To date, no LBG devices fabricated *via* sTE have been reported.

To achieve adequate light absorption, and thus optimal charge-generation density, the PVK layer must be 500–700 nm thick.[25] However, earlier work on Pb-based PVKs has reported that using sTE imposes an upper limit on the film thickness achievable in a single deposition cycle, a restriction attributed to limited interdiffusion of the deposited precursor layers. To overcome this, multi-cycle sTE was developed, where each cycle (c) consists of a full sequence of depositing all separate precursors.[30]

In this work, we report the successful deposition of LBG formamidinium lead tin triiodide ($FAPb_{0.5}Sn_{0.5}I_3$) films up to 700 nm using a single cycle (1c) of sTE. This method first involves the deposition of an in-house-prepared PbI_2–SnI_2 alloy layer, referred to as $PbSnI_4$, followed by a layer of formamidinium iodide (FAI). This approach produces near-intrinsic perovskites while eliminating the need for the additives that are normally required for solution-processed PVKs.[22] The resulting films are compositionally uniform throughout their thickness and display compact structures and well-defined columnar grains. By integrating these layers into functioning PSCs, achieving champion PCEs above 10%, we underscore the viability of 1c-sTE for scalable PVK absorber production.

Central to this study is understanding why this material can be produced in 1 cycle of sTE at such thicknesses. To address this, the differences between samples produced in a single cycle and those from a double cycle (2c) were examined, revealing that the 1c films exhibit superior structural and optoelectronic properties compared to their 2c counterparts. Furthermore, we thoroughly investigate the interdiffusion behavior of the $PbSnI_4$ and FAI precursor layers by characterizing the films at three stages during the production, both before and after annealing, using XRD, XPS, and solid-state NMR. Density-functional theory (DFT) calculations further reveal that the alloy is only weakly stabilized relative to its precursors and is energetically close to the mixed perovskite phase, facilitating lattice disruption and efficient interdiffusion. Finally, by comparing XRD and TRMC data of samples subjected to different annealing procedures, we establish that the diffusion of the precursors is not hindered by the concurrent crystallization into PVKs.

Experimental

$PbSnI_4$ alloy preparation

In an N_2-filled glovebox, tin(II) iodide beads (SnI_2, 99.999%) were ground and mixed with lead(II) iodide (PbI_2, 99.99%) in a 1 : 1 mol ratio. The mixture was transferred from the glovebox into the evaporator through ambient air. Afterward, the evaporation chamber was pumped down to 10^{-6} mbar and maintained in a vacuum overnight. Subsequently, an Ar flow was established through the chamber, and the crucible containing the mixture was slowly heated to 420 °C. After 20 minutes, the crucible was cooled to room temperature. The resulting alloy, denoted as $PbSnI_4$, was used in the perovskite deposition without further treatment.

Sequential thermal evaporation of perovskite layers

Quartz substrates were subsequently washed with acetone and isopropanol in an ultrasonic bath. Next, they were treated with oxygen plasma for 10 minutes. After loading them into the evaporation chamber, the substrates were swiftly heated to 40 °C in vacuum (10^{-7}–10^{-6} mbar) to ensure the removal of residual adherents. For the deposition of $FAPb_{0.5}Sn_{0.5}I_3$, sequential layers of $PbSnI_4$ and formamidinium iodide (FAI, 99.99%) were deposited onto a rotating substrate. The thicknesses for each layer are reported in Table S1.

Device preparation

Commercial ITO was cleaned with oxygen plasma for 10 minutes. Afterwards, poly(3,4-ethylenedioxythiophene):poly(styrene sulfonate) (PEDOT:PSS, PVP Al 4083) was deposited in the fume hood in ambient air by spincoating. The aqueous dispersion was first filtered using a 0.45 μm PVDF filter. 240 μL PEDOT:PSS was pipetted onto the substrate and spin-coated first with 500 rpm for 10 s, then with 4000 rpm for 30 s, both steps were performed with an acceleration of 12 000 rpm s^{-1}. The substrates were subsequently heated at 200 °C for 5 minutes at 200 °C in ambient conditions, after which they were taken into the glovebox to anneal for another 5 minutes at 200 °C. The substrates were then loaded into the evaporator, and 500 nm $FAPb_{0.5}Sn_{0.5}I_3$ perovskite films were deposited on top as described above. After the deposition, the samples were annealed for 30 minutes at 200 °C in the glovebox. Then the samples were transferred into a different evaporation system for the deposition of a 23 nm C60 layer and a 2 nm BCP layer. Then, 100 nm silver (Ag) contacts (0.09 cm^2) were deposited on top to finish the stack.

Structural characterization

X-ray diffraction (XRD). XRD measurements were performed on a Bruker D8 Advance-ECO diffractometer in Bragg–Brentano configuration using Cu Kα (λ = 1.54 Å) radiation. The measurements were done in ambient conditions. *In situ* XRD measurements were performed on a Bruker D8 Discover X-ray diffractometer in 1 bar of N_2 environment using an Anton Paar XRK900 Reactor chamber in Bragg–Brentano configuration. The measurements were performed using Cu Kα (λ = 1.54 Å) and a LYNXEYE XE detector operated in 0D mode. A fixed exit slit of 0.6 mm was used, and two 0.6 mm slits were used on the secondary side.

X-ray photoelectron spectroscopy (XPS). XPS measurements were done using a Thermo Scientific K-alpha system using Al Kα (1.49 keV, 8.34 Å) radiation in an ultra-high vacuum chamber (pressure < 10^{-8} mbar). The spot size was about 800 × 400 μm^2, the flood gun was operated at 0.15 mA and 1 V, and the pass energy was set to 140 eV. Depth profiles were constructed by etching the layer using an Ar^+ ion beam with an energy of 1 keV. The atomic ratios and depth profiles were obtained by fitting the XPS peaks using the ThermoAdvantage software.

Solid state nuclear magnetic resonance (ssNMR). Solid-state NMR measurements were performed on a Bruker Ascend 500 magnet (B_0 = 11.7 T) with a NEO console operating at frequencies of 104.64 MHz, 125.77 MHz, and 500.16 MHz for ^{207}Pb, ^{13}C and ^{1}H respectively. Chemical shifts were referenced with respect to solid $Pb(NO_3)_2$ (^{207}Pb −3474 ppm) and adamantane (^{1}H 1.81 ppm and ^{13}C 38.48 ppm). The samples were packed into 3.2 mm zirconia rotors and a Bruker three channel MAS 3.2 mm DVT probe was employed. Temperatures were regulated to 25 °C for all measurements. For the ^{207}Pb measurements, static spectra were recorded using the variable offset cumulative spectra (VOCS) approach. Hahn echo measurements were performed in different cumulative spectral ranges for each of the samples, varying the offset by 500 ppm each time. A 90° pulse length of 2.2 μs was used. An echo time of 19 μs was used for the mixed and annealed samples, while a shorter echo time of 10 μs was used for the alloy sample. Additional ^{207}Pb, ^{13}C and ^{1}H magic angle spinning NMR measurements were performed on the mixed and annealed samples. A MAS speed of 15 kHz was employed for ^{207}Pb and ^{1}H, while 12 kHz was used for ^{13}C. Here as well, ^{207}Pb spectra were recorded using the Hahn-echo sequence. The ^{1}H spectra were recorded using the one pulse (Bloch decay) sequence, and ^{13}C spectra using the hpdec sequence. 90° pulse lengths of 2.5 μs for ^{1}H and 3.5 μs for ^{13}C were determined. Appropriate recycle delays were utilized based on T1, which was determined with a saturation recovery experiment.

Scanning electron microscopy (SEM). SEM measurements were performed on a JEOL JSM-IT700 field effect microscope with an accelerating voltage of 5 keV. Cross-sectional SEM images were obtained by attaching the samples to a stub with a 45° slope. The images were taken on a 10° angle with respect to the sample surface.

Dektak stylus profilometry. The thickness of the films was determined using stylus profilometry, performed on a Veeco Dektak 8 profilometer.

Optoelectronic characterization

Absorption measurements. Absorption spectra were collected in ambient conditions in the integrated sphere on a Lambda 1050 spectrophotometer to determine the fraction of light that was either transmitted or reflected (F_{T+R}). Subsequently, the fraction of absorbed light (F_A) was calculated by $F_A = 1 - F_{T+R}$.

Photoconductance measurements. Microwave conductivity measurements were used to study the dark conductivity, the photoconductance and the QFLS of the perovskite films. In this technique, the reduction in microwave power is directly related to a change in conductivity. Detailed information about the technique is included in the SI.

Cell characterization

Current density–voltage (*J*–*V*) measurements. *J*–*V* measurements were performed by scanning between −0.1–0.9 V and measuring the current density response at a scan rate of 50 Hz using a Keithley 2604. A solar simulator (OAI TriSOLTM Large Area) was used to mimic the AM1.5 solar spectrum. The incident light intensity was 120 mW cm^{-2}.

Results

1c-sTE as a viable production method for PSC absorber layers

$FAPb_{0.5}Sn_{0.5}I_3$ was produced from an in-house synthesized $PbSnI_4$ alloy, formed by combining lead(II) iodide (PbI_2) and tin(II) iodide (SnI_2) in a 1 : 1 molar ratio. This alloy was sublimed first at a rate of 1.5 Å s^{-1}. In the subsequent step, a layer of formamidinium iodide (FAI) was deposited at a rate of 1.0 Å s^{-1}, following the procedure described in a previous publication.[22] While maintaining the same deposition rates, the overall PVK film thickness was increased from 250 nm to 700 nm by proportionally scaling the individual precursor layer thicknesses without the need for additional stoichiometric optimization, as is shown in Fig. S1A. The ability to scale up the process demonstrates the straightforward nature of the sTE process, for which tooling factors remain constant independent of deposition time and the amount of material already deposited. After the deposition, the films were removed from the evaporator and annealed at 200 °C on a hotplate in a N_2 environment for various durations. A schematic illustration of the sTE process is included in Fig. S1B.

It is imperative for this work to thoroughly check the interdiffusion of precursors before and after annealing, as there have been serious indications that there is a limit to the maximum film thickness that can be deposited in a single cycle (1c) using sTE with lead-based perovskites.[30] To test the distribution of various elements across the film thickness, a compositional depth profile of a sample annealed for 10 minutes was measured using X-ray photoelectron spectroscopy (XPS) (Fig. 1A). Most interestingly, 1c-sTE yields LBG PVK films with uniform stoichiometry throughout the entire thickness, indicating optimal interdiffusion between the PVK precursors. Even though the overall composition is constant, the measured atomic percentages deviate somewhat from the expected values (Table S2), particularly an underestimation of the A- and X-site species (N and I) relative to the B-site (Sn and Pb) metals. Table S3 presents the Pb : Sn : I ratio determined by XPS for all samples used in this study, confirming that the difference in detected halide and metal ion concentration is present throughout. These deviations are likely measurement artifacts, as nitrogen detection is known to be challenging in XPS. We also include XPS survey scans of the films' surfaces in Fig. S3 to verify that they contain no detectable impurities. Moreover, the top-view scanning electron microscopy (SEM) images in Fig. 1B show that the films appear compact, with grains larger than 3 μm, and do not contain pinholes. The presence of continuous grains throughout the film thickness is confirmed by side-view SEM measurements (Fig. 1C). It is noteworthy that achieving this type of film morphology *via* spincoating is highly challenging and typically requires extensive additive engineering.[8,11,31–33] Collectively, the XPS and SEM results demonstrate that films fabricated using 1c-sTE are stoichiometrically homogeneous, pinhole-free, and continuous, making them ideal for PV applications.

To further demonstrate the feasibility of the 1c-sTE process, a 500 nm thick absorber layer was incorporated into a device with the architecture ITO/PEDOT:PSS/$FAPb_{0.5}Sn_{0.5}I_3$/C60/BCP/Ag (Fig. 1D). The current–voltage characteristic of a champion cell based on this architecture, obtained using a solar simulator with an output power of 120 mW cm^{-2}, is shown in Fig. 1E, yielding a power conversion efficiency (PCE) of 10.2%. This performance results from a short-circuit current density (J_{SC}) of 30.5 mA cm^{-2}, a fill factor (FF) of 65%, and an open-circuit voltage (V_{OC}) of 0.62 V. More performance parameters are included in the top row of Table S4. Although previous work from Valencia[25] indicates that 700 nm LBG PVK layers are too thick, leading to reduced charge collection and increased parasitic absorption, we nevertheless fabricated cells with this PVK film thickness as well. A champion *J–V* is included in Fig. S4A. As expected, the increased absorption (shown for each thickness in Fig. S4B) leads to a rise in current, yielding a J_{SC} of 35.2 mA cm^{-2}, while the V_{OC} and FF a decrease to 0.55 eV and 61%, respectively. As is also indicated in Table S4, this results in a comparable PCE of 9.8%. While the PCE we obtain is equivalent to previously reported values for solar cells containing evaporated Pb–Sn perovskite absorbers,[23–25] the individual performance parameters are notably different.

To identify the origin of the low device voltage and the apparent difficulties in extracting charges to the contacts, we performed QFLS measurements using light intensities comparable to 1 sun. The QFLS of bare PVK layers (0.82 eV) is compared with those of stacks incorporating an HTL, an ETL, or both. This method has been widely used in literature[10,34–37] and is most effective for identifying voltage losses that occur at the interfaces between the PVK and the TLs. The QFLS values are also included in Table S5. Fig. 1F shows that, after depositing the ETL (C60) on top, the QFLS increases slightly from 0.82 to 0.87 eV. This is an uncommon outcome, as this interface typically introduces voltage losses.[37] In contrast, a significant voltage loss is observed when the perovskite is deposited on PEDOT:PSS (HTL), as the QFLS drops to 0.71 eV. The QFLS of the full HTL/PVK/ETL stack closely matches that of the HTL/PVK stack, reaching 0.69 eV. The remaining discrepancy between the device V_{OC} and the QFLS of the triple layer may be attributed to sheet resistance in the ITO and/or collection losses at the metal contacts. In short, the PSC produced *via* 1 cycle of sTE is effective, but its device architecture, particularly the selection of charge transport layers, needs improvement.

On the ease of mixing in sTE-produced $FAPb_{0.5}Sn_{0.5}I_3$

Having successfully integrated the 1c-produced PbSn PVKs perovskites into a PSC, we now turn to understanding the conversion, meaning the mixing of the precursors and crystallization into the PVK phase. Moreover, we investigate why these processes proceed to completion in this system, whereas they are hampered in pure-Pb PVKs.[30] We first compare films deposited in 1c to those prepared using a double cycle (2c) of sTE to gain insight into how the different deposition approaches influence precursor diffusion, crystallization, and the resulting film properties. In these experiments, a total thickness of 700 nm was maintained. The individual layer

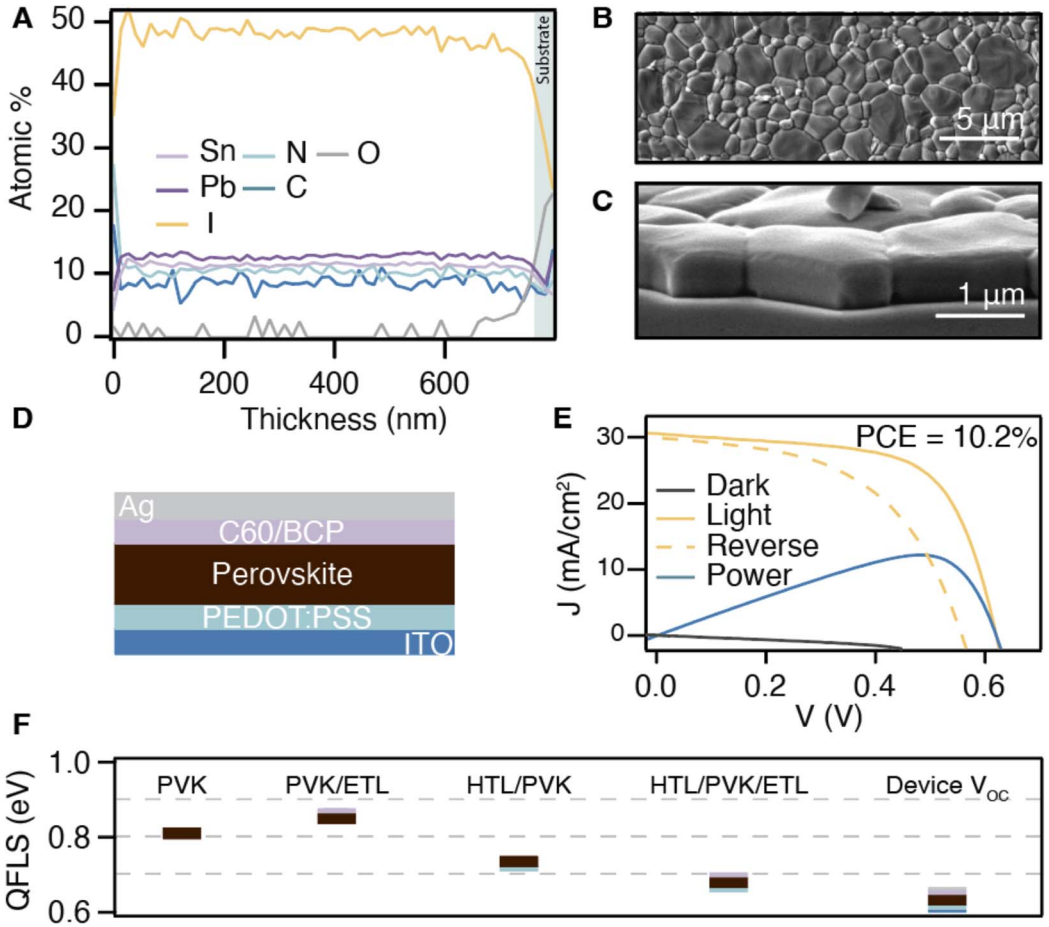

Fig. 1 (A) Compositional XPS depth profiles showing the atomic percentage (%) as a function of the layer thickness (nm) of $FAPb_{0.5}Sn_{0.5}I_3$ PVK films deposited in a single cycle of sequential thermal evaporation. (B) Top-view SEM image of an annealed PVK film. The scale bar indicates 5 µm. (C) Cross-sectional SEM images of an annealed PVK film. The scale bar indicates 1 µm. All samples used were annealed for 30 minutes at 200 °C. (D) Schematic representation of the device architecture used in this work, consisting of ITO/PEDOT:PSS/$FAPb_{0.5}Sn_{0.5}I_3$/C60/BCP/Ag. (E) *J*–*V* and power characteristic of the champion cell employing 500 nm thick PVK films. The reverse scan is also included. (F) Quasi-Fermi level splitting (QFLS) of the bare PVK film as well as the partial stacks with the HTL (PEDOT:PSS) and the ETL (C60). Plotted together with the device open-circuit voltage (V_{OC}).

thicknesses are reported in Table S1. The samples were annealed at 200 °C for varying times (10–60 minutes).

The XRD patterns (Fig. 2A and B) show minimal differences between the two methods, with both exhibiting a preferential orientation, dominated by reflections at 14.0° and 28.2°, corresponding to the (100) and (200) crystal planes of the perovskite phase, respectively. Additionally, annealing for longer durations (>30 min) at 200 °C leads to the emergence of an alloy peak at 12.7°, indicating thermal degradation and reversion into the precursor. Notably, the 2c approach shows additional reflections from other crystal planes, specifically with a more pronounced (012) reflection at 31.6°. The differently oriented perovskite domains likely result from the second deposition cycle being performed on a different surface than the first. Namely, the second cycle is performed on a layer of non-crystalline FAI rather than directly on quartz. This change in substrate could influence the nucleation and growth process, thereby affecting the resulting crystal orientation.[38,39]

Moreover, the absorbance spectra, (F_A), in Fig. 2C and D show that the bandgap of the perovskites prepared *via* both approaches is approximately 1.28 eV, suggesting identical compositions and phases. Interestingly, the spectra show that the 2c films require more time to convert into the same amount of absorbing material as the 1c films. In the 1c approach, the absorbance saturates after just 10 minutes of annealing, whereas full conversion in the 2c films occurs only after about 30 minutes. These findings indicate that films produced using a double cycle of sTE undergo a prolonged crystallization pathway relative to those produced *via* a single cycle.

The XPS depth profile of a 2c-produced sample, shown in Fig. S2C, shows a similar uniformity of the elements across the film thickness, yet it differs somewhat from that of the 1c-produced film as it exhibits a higher overall formamidinium (N) content. This may be due to the second cycle being deposited on top of the first layer of FAI, which could prevent any excess material from desorbing during annealing.

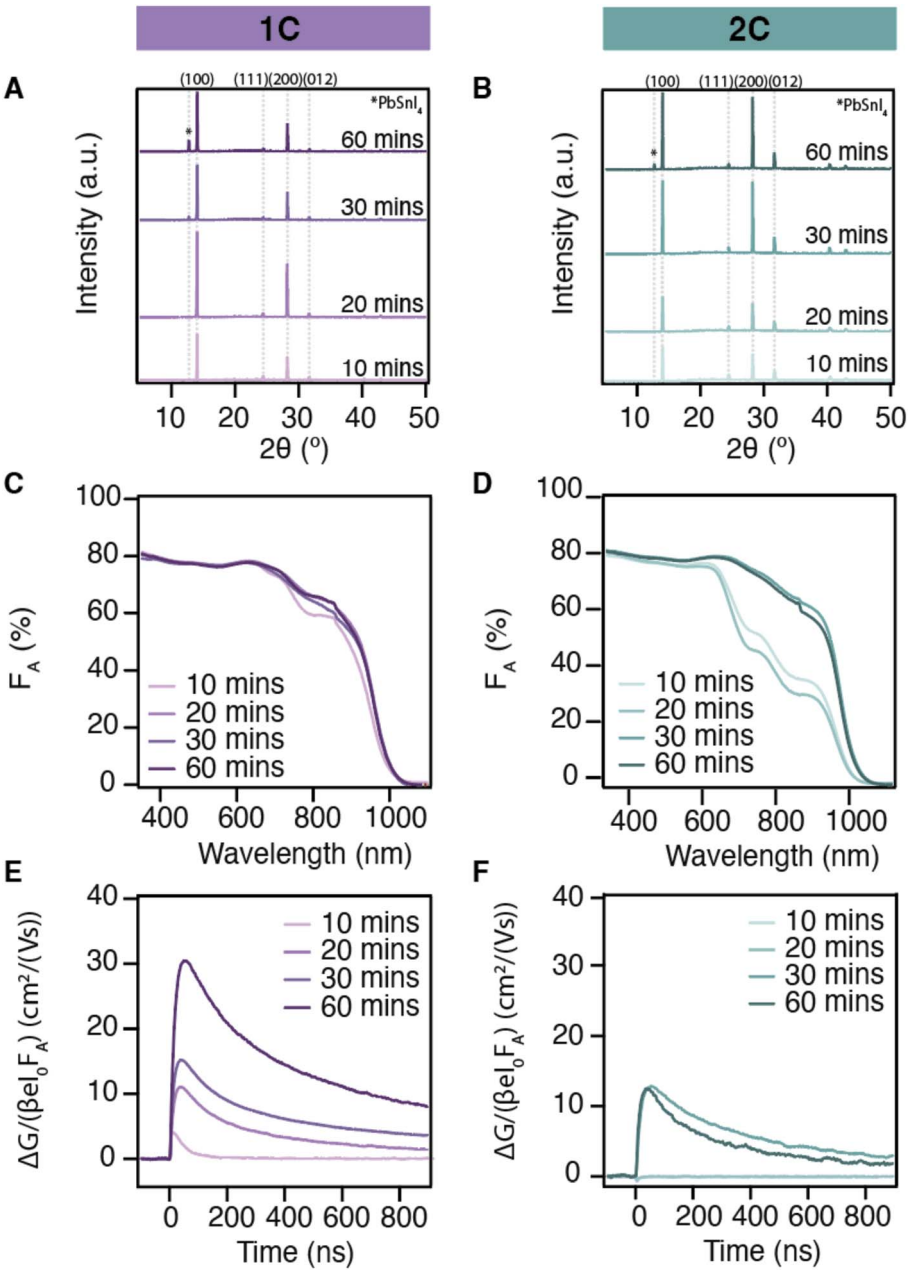

Fig. 2 XRD patterns of $FAPb_{0.5}Sn_{0.5}I_3$ perovskite films deposited in (A) a single cycle (1c) and (B) a double cycle (2c) of sequential thermal evaporation. Absorption spectra, expressed as the fraction of absorbed light (F_A, %) of the (C) 1c deposition and (D) 2c deposition. Time-resolved photoconductance measurements of the (E) 1c deposition and (F) 2c deposition. The photoconductance (ΔG) is normalized by a geometric factor (β), the elementary charge constant (e), the intensity of the incoming light pulse, and F_A. All measurements were carried out on samples that were annealed for 10, 20, 30, and 60 minutes, and using light intensities of 10^{10} photons per cm^2.

The morphology of PVK layers produced *via* the 1c and 2c processes was further examined using top- and cross-sectional electron micrographs, provided in Fig. S5 and S6 for films annealed for varying durations. Similar to the 1c films, the 2c-produced layers display compact structures with no visible pinholes and feature large grains (>2 μm) across all annealing times. The 2c-produced films also exhibit columnar grains, like the 1c films, and no signs of the double cycle are visible in the film cross-section (Fig. S6B). Overall, these results indicate that the film microstructure is largely comparable between the two approaches and that during annealing, the layers deposited in separate cycles coalesce into a single grain extending throughout the entire sample thickness.

Despite the similar structural properties, bandgaps, and film morphologies, the films fabricated by these approaches display notable differences in photoconductance, which was evaluated using time-resolved microwave conductivity (TRMC) measurements. TRMC is a contactless technique that quantifies the sample conductance by measuring the decrease in microwave power resulting from interactions with mobile carriers

generated under photoexcitation, see the SI for a more detailed description. The photoconductance (ΔG) traces are normalized by a geometric factor (β), the electronic charge constant (e), the incident light intensity (I_0), and F_A, to express the data as a yield-mobility product. The data, presented in Fig. 2E and F for a light intensity of 10^{10} photons per cm^2, reveal that the 1c films exhibit progressively larger ΔG with annealing time, ultimately reaching maximum signals around 30 cm^2 (Vs^{-1}). In contrast, similarly to the evolution of the absorption, the 2c films show an increase only after 20 minutes of annealing, and the maximum ΔG remains below 15 cm^2 (Vs^{-1}).

All in all, these results demonstrate that while the 1c and 2c approaches ultimately yield structurally and morphologically comparable PVK films with similar bandgaps, their crystallization pathways differ. Counterintuitively, the 2c process exhibits slower conversion kinetics, which could be due to differences in precursor distribution during annealing. The reduced photoconductance response in the 2c films indicates that subtle differences in the films affect the electronic performance. These findings highlight that, beyond the benefits of shorter processing times and relative simplicity, the 1c-sTE films exhibit faster conversion and higher photoconductance with shorter annealing times. In this context, the homogeneous ion distribution observed in the XPS data (Fig. 1A) raises questions regarding the diffusion and crystallization processes in these films that lead to such uniformity. To address this, we further investigate the conversion by examining the structural and optical properties at three stages of 1c production. First, we characterize a sample immediately (<15 min) after the FAI deposition without annealing (in yellow). Another sample, denoted as mixed (in orange), was left unannealed for approximately 12 hours at room temperature in the glovebox. These layers are compared with a sample annealed for 30 minutes at 200 °C right after the FAI deposition (in burgundy).

The film images included in the key (Fig. 3A) already illustrate the extent of diffusion and crystallization at room temperature. The film's appearance changes from a bright orange hue directly after FAI deposition, characteristic of the $PbSnI_4$ alloy, to black by the next day. The absorption data in Fig. 3B tell a similar story: the unannealed material initially exhibits a shallow absorption onset, which develops remarkably over the 12 hours period the film is left in the glovebox, ultimately showing a distinct onset around 1000 nm. Comparatively, the difference in absorption around the band edge between the mixed film and the annealed sample is small. The identical absorption onsets observed for PVK formed spontaneously overnight and by annealing indicate that both contain a substantial amount of $FAPb_{0.5}Sn_{0.5}I_3$. These results show that even at room temperature, diffusion and crystallization occur, yielding a PVK phase with structural and optical properties similar to the annealed films.

The conversion from precursors to the desired perovskite phase can also be followed through the structural properties using XRD. Fig. 3C presents the diffraction patterns for the three studied samples. Directly after deposition, the film exhibits strong reflections at 12.7°, 25.5°, and 38.7°, which are characteristic of $PbSnI_4$,[22] and only minor PVK peaks at 14.0° and 28.2°. In contrast, the mixed sample shows only the perovskite-related reflections and none of the alloy. To track the progressive diffusion and crystallization of the precursors, the sample was monitored by XRD at 15 minutes intervals (Fig. 3D). Over a 12 hours time window, the alloy reflection at 12.7° gradually fades, while a broad (100) PVK peak at 14.0° develops. Upon annealing, the characteristic perovskite peaks remain visible in Fig. 3C, accompanied by a small alloy peak at 12.7°, which indicates minor degradation during annealing. A magnified view of the normalized (100) reflections of the resulting PVK films is shown in Fig. 3E. The as-deposited PVK portrays the widest peak, which narrows after mixing. Subsequent annealing for 30 minutes at 200 °C sharpens the peak, indicating an improvement in the crystallinity or increased crystallite sizes.

To study the conversion process in more detail, solid-state nuclear magnetic resonance (ssNMR) measurements were carried out to monitor the local environment of the Pb. Because mixing of the precursors occurs too rapidly, even at room temperature, in relation to the measurement time, it was not feasible to analyze an unannealed sample directly after the FAI deposition. Instead, the $PbSnI_4$ alloy was included. To accommodate the broad range of chemical shifts in which the NMR signal was obtained, the measurements for ^{207}Pb were performed using the variable offset cumulative spectra (VOCS) approach. The resulting static ^{207}Pb ssNMR spectra are shown in Fig. 3F–H, plotted together with the sum of the spectra in grey. Normalized magic-angle spinning (MAS) ^{1}H and ^{13}C spectra are included in Fig. S7. The $PbSnI_4$ ^{207}Pb spectrum exhibits a particularly broad peak spanning roughly −3000 to 4900 ppm (Fig. 3F). After overnight mixing, the peak narrows and centers at ~1647 ppm. Smaller peaks appear at 0 ppm and ~857 ppm. Subsequent annealing results in additional narrowing, producing a sharp peak at ~1788 ppm.

Several factors may account for the broad chemical shift distribution observed for $PbSnI_4$. For instance, variations in bond lengths or distortions of the lattice structure create asymmetric electron densities. Considering that the alloy was formed by thermally fusing PbI_2 and SnI_2, it is expected to exhibit both compositional inhomogeneities and structural disorder. This reasoning is corroborated by the broad X-ray reflection of the alloy, spanning between 12.3° and 13.0° in Fig. 3D, which is indicative of a distribution in lattice spacings.

We attribute the main peak in Fig. 3G to the $FAPb_{0.5}Sn_{0.5}I_3$ phase. Its higher chemical shift, which is above the ~1500 ppm typically reported for $FAPbI_3$,[40,41] indicates a lower electron density surrounding the Pb nuclei. The signal around 0 ppm has previously been associated with PbI_2,[41] suggesting that similar local environments may be present in our mixed material. The broad feature observed between 0 and 2000 ppm remains unidentified; it may result from sample heterogeneity, *i.e.*, a nonuniform Pb/Sn distribution, or the possible formation of some oxide species that could have formed during transport and characterization. Regardless, annealing evidently plays a major role in enhancing the symmetry of the electron densities surrounding the Pb nuclei in the PVK, which may indicate increased symmetry in the microdistribution of Sn and Pb. This

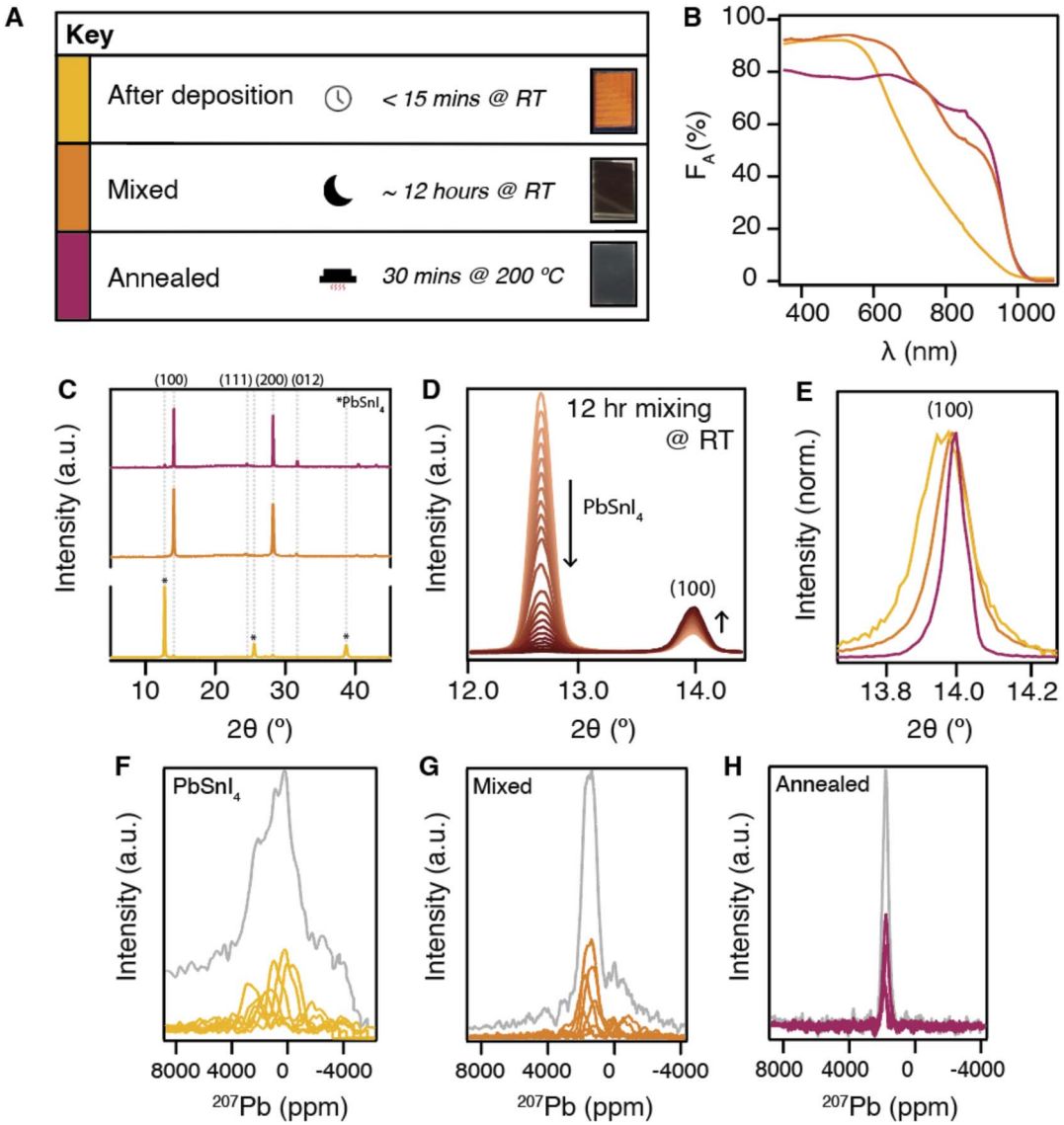

Fig. 3 (A) Key illustrating the different samples: a film measured within 15 minutes after the deposition (in yellow), an unannealed film left to mix overnight (in orange), and a film annealed directly after the deposition for 30 minutes at 200 °C (in burgundy). Pictures of the resulting films are also included. For all samples, the (B) absorption spectra, expressed as a fraction of absorbed light (F_A) of the samples introduced in the key, and (C) XRD patterns are included. (D) XRD patterns, zoomed in on the alloy peak (at 12.7°) and the PVK (100) (at ~14.0°), taken every 30 minutes over the course of 12 hours while the sample was kept in a N_2 environment at room temperature (RT). (E) Magnification of the (100) peak of the samples introduced in the key. Static ^{207}Pb Solid-state NMR (ssNMR) spectra of (F) $PbSnI_4$, (G) mixed, and (H) annealed sample. The different spectra in each subfigure correspond to measurements with different frequency offsets to cover the wide spectral range. The sum of each of these spectra for each sample is plotted in grey.

is reflected in the substantial narrowing of the main peak in Fig. 3H and the disappearance of the broad secondary signals.

Finally, top-view SEM images reveal pronounced changes in the films' microstructure across the different stages of the conversion. The as-deposited alloy (Fig. S8A) exhibits a compact morphology composed of small grains (<100 nm). After overnight mixing (Fig. S8B), the PVK film maintains the nanoscale features (<100 nm), but with visible voids distributed throughout the structure. Upon annealing, these features turn into large grains exceeding 1 μm in size (Fig. S5).

From the combined SEM, ssNMR, XRD, and absorption results, it can be concluded that evaporated FAI can disrupt the alloy's structure sufficiently to permit complete diffusion, leaving a void-rich film with no $PbSnI_4$ crystalline domains detectable by XRD. In time, a substantial amount of the desired $FAPb_{0.5}Sn_{0.5}I_3$ PVK phase forms even at room temperature. Nevertheless, annealing is essential to obtain PVK crystallites with a high degree of symmetry in the elemental distributions and large grains.

To further evaluate the thermodynamic stability of the $PbSnI_4$ alloy and to clarify why FAI seems to diffuse so readily,

detailed DFT calculations were performed. Using the total energies from DFT, the stability of the $PbSnI_4$ alloy was first assessed *via* the synthesis reaction $PbI_2 + SnI_2 \rightarrow PbSnI_4$. This reaction has an energy change $\Delta E = -0.103$ eV, corresponding to −0.017 eV per atom, showing that the alloy is only weakly stabilized with respect to its precursors. The modest energy gain indicates that the $PbSnI_4$ network is thermodynamically shallow and can be readily reconfigured when additional species are introduced at the processing temperatures used here.

The perovskite $FAPb_{0.5}Sn_{0.5}I_3$ was then evaluated using the same energy reference framework. Its formation energy is +0.0217 eV per atom, meaning that $FAPb_{0.5}Sn_{0.5}I_3$ is only about 0.039 eV per atom less stable than the $PbSnI_4$ alloy. The energy difference of 0.039 eV per atom is small compared to the thermal energy available at the annealing temperature (∼200 °C), so the alloy and perovskite have similar thermodynamic stabilities and can be interconverted under the processing conditions. Under the FAI-rich environment during deposition and annealing, entropic and interfacial effects, together with the chemical driving force for FA^+ incorporation, readily overcome this small energetic offset and enable extensive conversion of $PbSnI_4$ into $FAPb_{0.5}Sn_{0.5}I_3$.

This energetic picture aligns with the experimental observations that once FAI is deposited on top of the alloy, the $PbSnI_4$ lattice is easily disrupted. Most importantly, this allows the FAI to diffuse through the entire 500–700 nm film, and a substantial fraction of the perovskite phase forms already during room-temperature mixing. Together, the calculations support the view that $PbSnI_4$ acts as a structurally soft, weakly stabilized precursor that can be converted efficiently into the mixed Pb–Sn perovskite phase during single-cycle sequential thermal evaporation.

Finally, it remains to be determined whether diffusion of FAI into $PbSnI_4$ is influenced by simultaneous crystallization. To address this, a sample was annealed immediately after deposition, denoted as unmixed, and compared with a sample annealed after a day of spontaneous mixing at room temperature, denoted as mixed. The different sample treatments are schematically indicated in the top panels of Fig. 4. Given that the mixed sample already has a substantial amount of PVK and a uniform FAI distribution before annealing (see the compositional depth profiles in Fig. S2A), no additional diffusion should be necessary for full crystallization to the PVK phase. In contrast, for the unmixed sample immediately after deposition, FAI and $PbSnI_4$ remain spatially separated, and mixing occurs during annealing. The difference between the samples' initial state is also evident in the two XRD patterns of the unannealed films in Fig. 4A and B, consistent with the spontaneous overnight mixing discussed in Fig. 3. Tracking the evolution of the XRD patterns together with the photoconductance at various annealing times (0, 10, 20, 30, and 60 minutes) allows us to assess whether FAI transport during annealing influences crystallization and the resulting charge carrier dynamics.

As shown in Fig. 4A and B, the XRD patterns of the samples reveal similar diffraction peaks after annealing. In both cases, annealing for 10 minutes yields the characteristic reflections of $FAPb_{0.5}Sn_{0.5}I_3$ with no remaining alloy peaks. The alloy reflections re-emerge only after annealing for >20 minutes, indicative of thermal degradation.

From the TRMC data in Fig. 4C and D, it is evident that, for both annealing approaches, extending the annealing time to 60 minutes considerably improves the photoconductance, yielding a maximum signal around 80 cm^2 (Vs^{-1}) at a light intensity of 9 × 10^{10} photons per cm^2. This is striking as before annealing, the films differ substantially; the unmixed sample shows basically no photoconductance immediately after deposition, while a small but persistent photoconductance signal is observed in the mixed sample, attributable to the spontaneously formed PVK (Fig. S9). Interestingly, the evolution of the photoconductance signals with annealing time is remarkably similar for both preparation approaches. After 10 minutes of annealing, the signal peaks at 2–3 cm^2 (Vs^{-1}) and increases to 15–25 cm^2 (Vs^{-1}) after 20 minutes. Here, lifetimes of around 150–250 ns are observed. At 30 minutes of annealing, the photoconductance decreases slightly, yet the carrier lifetimes extend to 700 ns. Further annealing to a total of 60 minutes increases the signal height and prolongs the lifetimes to beyond 4 μs, as shown more clearly in Fig. S9. This enhancement correlates with the reappearance of the $PbSnI_4$ alloy peak at 12.7° in the XRD pattern in Fig. 4A and B. An excess of inorganic precursor has been associated with effective grain boundary passivation, resulting in longer-living photoconductance signals, albeit typically accompanied by lower device performances.[42–44]

The TRMC data also contains information regarding the defect density in the material. Fig. S10 presents TRMC signals for both samples, recorded at different light intensities. After 10 minutes of annealing, the rapidly decaying traces overlap across all excitation intensities. This behavior indicates that the charge carrier generation density remains below the trap density of the film, resulting in the same transient photoconductance signals regardless of the applied laser intensity.[45] Accordingly, the trap density can be estimated from the laser pulse intensity at which the traces stop to overlap. In this case, after correcting for the sample thickness, we find this to be greater than 10^{15} cm^{-3}. With annealing times beyond 10 minutes, the traces no longer overlap. Instead, the signals lower altogether with increasing laser pulse intensity. This suggests the emergence of a dominant second-order band-to-band recombination, which occurs once the trap density has been exceeded. Hence, it can be concluded that the trap density lowers significantly from >10^{15} cm^{-3} to around 10^{13} cm^{-3} upon annealing. This trend is observed for films produced *via* both approaches presented in Fig. 4.

Additional information about the annealing process in the films is provided by dark microwave conductivity (DMC) measurements, in which the GHz response is recorded as a function of resonance frequency. As shown in Fig. S11, a clear difference in microwave interactions is observed between the unannealed samples. For the unmixed sample, the normalized resonance dip reaches a minimum of approximately 0.63, whereas for the mixed sample, the dip deepens to 0.39. Dip deepening in DMC is associated with increased background conductivity. Upon annealing, the resonance dips in both cases shift to approximately 0.51 after 10 minutes and subsequently

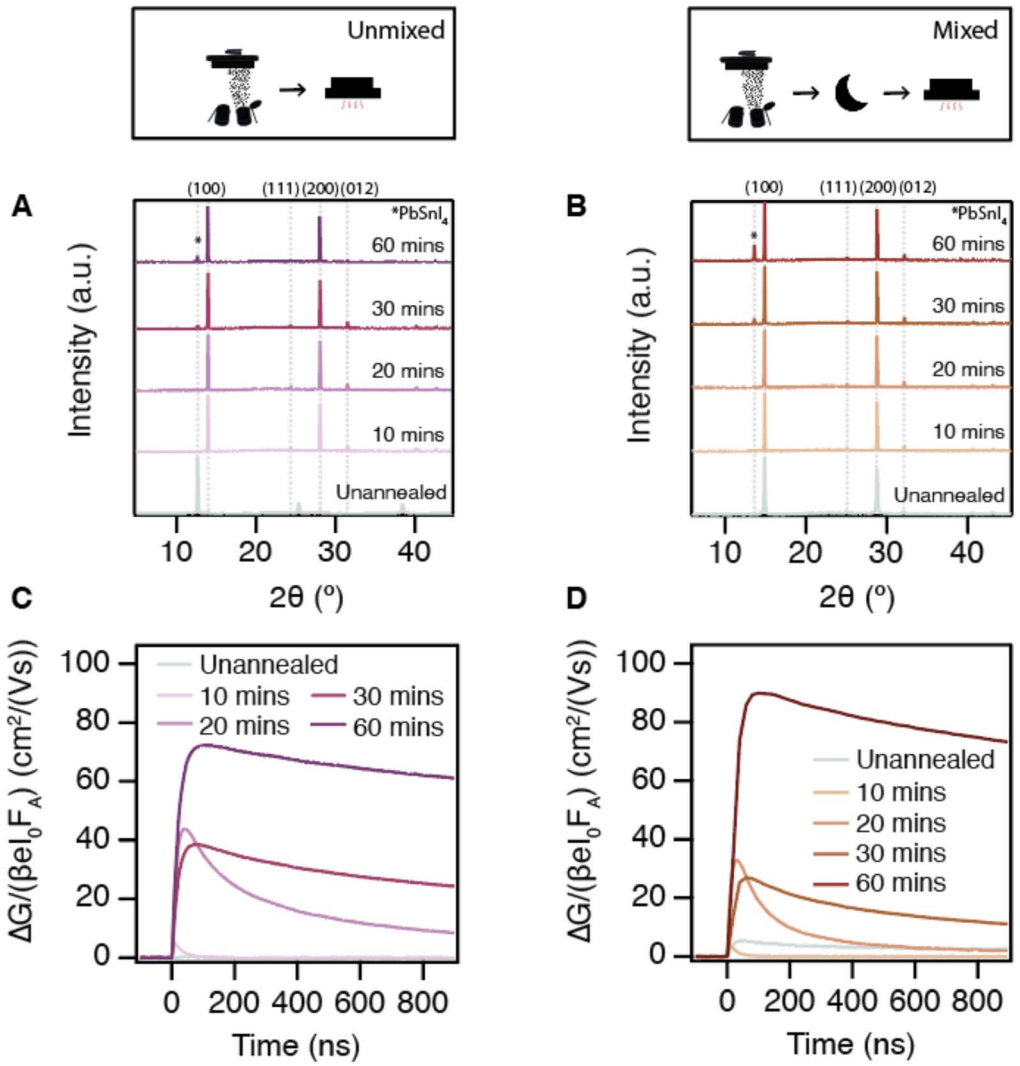

Fig. 4 XRD patterns of perovskite films left unannealed and annealed at 200 °C for varying times (A) immediately after the deposition, and (B) after overnight mixing. Photoconductance traces as a function of time for perovskite films annealed at 200 °C, (C) immediately after the deposition, and (D) after overnight mixing. The annealing timing is also schematically indicated in the panels above the TRMC traces. The ΔG signals are reported for different annealing times (10, 20, 30 and 60 minutes) and using a light intensity of 9×10^{10} photons per cm^2.

become shallower, reaching around 0.6 after 60 minutes. This is comparable to the substrate, implying that annealing reduces the background conductivities to < 1 S m^{-1}. From this and the fact that the charge carrier mobility only increases, we can conclude that the initially present doping concentrations, in particular for the mixed sample, are neutralized by the annealing process.

Based on the similarities in the evolution of the TRMC signals and structural properties during annealing, we can infer that the PVK films are in equivalent stages of conversion at each time step. Hence, the diffusion is not significantly hampered by simultaneous crystallization and is either very rapid or proceeds independently of the crystallization process at these high temperatures.

Despite the close agreement in diffraction patterns and transient photoconductance, we decided to fabricate PSCs using the mixed PVK films. The *J–V* characteristic of a champion device is included in Fig. S12A. In line with the TRMC findings, the two fabrication approaches yield nearly indistinguishable performance. The devices based on mixed PVK layers achieve a champion PCE of 10.3%, composed of a J_{SC} of 30.9 mA cm^{-2}, a V_{OC} of 0.61 V, and a FF of 66%. The device parameters are also included in Table S4. Likewise, we find almost identical QFLS values for both deposition approaches for the bare PVK film as well as the PVK/ETL, HTL/PVK, and HTL/PVK/ETL stacks, which are also included in Fig. S12B and listed in Table S5. As noted above, the major voltage losses appear at the HTL/PVK interface. In the future, approaches incorporating carbazole-based materials like (2-(9*H*-carbazol-9-yl)ethyl)phosphonic acid (2PACz), which have recently shown significant success,[46,47] represent a more promising approach.

Taken together, the findings on the diffusion and crystallization presented in Fig. 3 and 4 indicate that FAI and $PbSnI_4$ readily mix and convert into the PVK phase at room

temperature, consistent with the thermodynamically shallow stability of this system. Although the mixed PVK is macroscopically homogeneous, as evidenced by X-ray reflections and a uniform elemental distribution throughout the film's thickness, it is modestly doped. For both samples, annealing is required to achieve films with increased local homogeneity, large grains, and high crystallinity. These structural changes lead to a reduction in defect density and increased carrier mobility, along with longer lifetimes. For mixed samples, annealing substantially reduces the background conductivity. Hence, for electronic activation, high temperatures are essential. We speculate that this is related to the repositioning of the larger, less mobile ions, such as Sn^{2+} and Pb^{2+}, to improve the elemental distribution at the microscale.

Conclusion

All in all, we demonstrate the scalable fabrication of low bandgap Pb–Sn perovskite films up to 700 nm thick using a single cycle of sequential thermal evaporation. The resulting films are stoichiometrically uniform throughout their thickness and exhibit large, columnar grains with a compact morphology. A detailed investigation of the crystallization and diffusion processes during the production of these perovskites revealed that, after the vacuum deposition, the precursors readily mix when the samples are left in the glovebox overnight. Additionally, the desired $FAPb_{0.5}Sn_{0.5}I_3$ phase gradually forms over time. We attribute this behavior to the relatively weak thermodynamic stabilization of the PVK phase compared to the precursors. Moreover, we conclude that annealing is essential to achieve films with improved elemental homogeneity on basis of the ssNMR, large grains, and high crystallinity. These improvements lead to reduced defect density, increased carrier mobilities up to 80 cm^2 (Vs^{-1}), and longer lifetimes as determined by dark and time-resolved microwave techniques. When integrated into solar cells with the architecture ITO/PEDOT:PSS/$FAPb_{0.5}Sn_{0.5}I_3$/C60/BCP/Ag, they achieved champion efficiencies of 10.3%, with observed voltage losses predominantly originating from the interface with the PEDOT:PSS HTL. In conclusion, this work contributes to the development of large-scale fabrication methods for low bandgap perovskite films using thermal evaporation, highlighting their potential for commercialization as high-performance absorber layers.

Author contributions

L. P., A. S., and T. S. designed and supervised the project. M. D. and L. P. prepared the samples, with the assistance of R. B and N. S., and conducted XRD, UV-vis, SEM, XPS, IV, and microwave conductivity measurements. L. B. and L. P. measured *in situ* XRD. P. V and D. G. performed and analyzed the DFT calculations. S. G and L. B. performed and analyzed the ssNMR measurements. L. P and T. S. wrote the manuscript, with the input of the remaining authors.

Conflicts of interest

There are no conflicts to declare.

Data availability

The data supporting this article have been included as part of the supplementary information (SI). Supplementary information: Tables S1–S5, Fig. S1–S12, and further experimental details regarding the TRMC measurements. See DOI: https://doi.org/10.1039/d6el00044d.

Notes and references

1 National Renewable Energy Laboratory, Best Research-Cell Efficiencies, 2023, https://www.nrel.gov/pv/cell-efficiency.html.
2 R. Lin, *et al.*, All-perovskite tandem solar cells with 3D/3D bilayer perovskite heterojunction, *Nature*, 2023, **620**, 994–1000, DOI: 10.1038/s41586-023-06278-z.
3 J. Liu, *et al.*, Perovskite/silicon tandem solar cells with bilayer interface passivation, *Nature*, 2024, **635**, 596–603, DOI: 10.1038/s41586-024-07997-7.
4 X. Liu, *et al.*, Charge carrier management for highly efficient perovskite/Si tandem solar cells with poly-Si based passivating contacts, *Energy Environ. Sci.*, 2025, **18**, 5599–5609, DOI: 10.1039/d5ee01486g.
5 Z. Liu, *et al.*, All-perovskite tandem solar cells achieving >29% efficiency with improved (100) orientation in wide-bandgap perovskites, *Nat. Mater.*, 2025, **24**, 252–259, DOI: 10.1038/s41563-024-02073-x.
6 F. Huang, M. Li, P. Siffalovic, G. Cao and J. Tian, From scalable solution fabrication of perovskite films towards commercialization of solar cells, *Energy Environ. Sci.*, 2019, **12**, 518–549, DOI: 10.1039/c8ee03025a.
7 Y. Zhao, *et al.*, Research progress in large-area perovskite solar cells, *Photon. Res.*, 2020, **8**, 1848–1865, DOI: 10.1364/prj.392996.
8 Z. Saki, M. M. Byranvand, N. Taghavinia, M. Kedia and M. Saliba, Solution-processed perovskite thin-films: the journey from lab- to large-scale solar cells, *Energy Environ. Sci.*, 2021, **14**, 5690–5722, DOI: 10.1039/d1ee02018h.
9 F. Yang, *et al.*, Upscaling Solution-Processed Perovskite Photovoltaics, *Adv. Energy Mater.*, 2021, **11**, 2101973, DOI: 10.1002/aenm.202101973.
10 K. Zhang, *et al.*, Suppressing Nonradiative Recombination in Lead–Tin Perovskite Solar Cells through Bulk and Surface Passivation to Reduce Open Circuit Voltage Losses, *ACS Energy Lett.*, 2022, **7**, 3235–3243, DOI: 10.1021/acsenergylett.2c01605.
11 H. Lee, S. B. Kang, S. Lee, K. Zhu and D. H. Kim, Progress and outlook of Sn–Pb mixed perovskite solar cells, *Nano Converg.*, 2023, **10**, 21, DOI: 10.1186/s40580-023-00371-9.
12 H. Wang, *et al.*, Additive Engineering for Mixed Lead–Tin Narrow-Band-Gap Perovskite Solar Cells: Recent Advances and Perspectives, *Energy Fuels*, 2023, **37**, 6401–6423, DOI: 10.1021/acs.energyfuels.3c00462.

13 J. Yan, T. J. Savenije, L. Mazzarella and O. Isabella, Progress and challenges on scaling up of perovskite solar cell technology, *Sustain. Energy Fuels*, 2022, **6**, 243–266, DOI: 10.1039/d1se01045j.
14 Y. Vaynzof, The Future of Perovskite Photovoltaics—Thermal Evaporation or Solution Processing?, *Adv. Energy Mater.*, 2020, **10**, 2003073, DOI: 10.1002/aenm.202003073.
15 Z. Wang, *et al.*, Thermally Evaporated Metal Halide Perovskites and Their Analogues: Film Fabrication, Applications and Beyond, *Small Methods*, 2024, **9**, 24001633, DOI: 10.1002/smtd.202301633.
16 T. Feeney, *et al.*, High-Rate FA-Based Co-Evaporated Perovskites: Understanding Rate Limitations and Practical Considerations to Overcome Their Impact, *Adv. Funct. Mater.*, 2025, **35**, 2517873, DOI: 10.1002/adfm.202517873.
17 R. K. Boekhoff, *et al.*, Interplay of cross-reading, pressure and co-evaporation speed on triple-source FA-based perovskite films and devices, *Chem. Eng. J.*, 2026, **530**, 173755, DOI: 10.1016/j.cej.2026.173755.
18 C. Momblona, *et al.*, Efficient vacuum deposited p-i-n and n-i-p perovskite solar cells employing doped charge transport layers, *Energy Environ. Sci.*, 2016, **9**, 3456–3463, DOI: 10.1039/c6ee02100j.
19 J. Li, *et al.*, Highly Efficient Thermally Co-evaporated Perovskite Solar Cells and Mini-modules, *Joule*, 2020, **4**, 1035–1053, DOI: 10.1016/j.joule.2020.03.005.
20 M. Ross, *et al.*, Co-Evaporated p-i-n Perovskite Solar Cells beyond 20% Efficiency: Impact of Substrate Temperature and Hole-Transport Layer, *ACS Appl. Mater. Interfaces*, 2020, **12**, 39261–39272, DOI: 10.1021/acsami.0c10898.
21 H. Li, *et al.*, Sequential vacuum-evaporated perovskite solar cells with more than 24% efficiency, *Sci. Adv.*, 2022, **8**, eabn8917, DOI: 10.1126/sciadv.abo7422.
22 L. M. van der Poll, *et al.*, Additive-Free Sequential Thermal Evaporation of Near-Intrinsic Pb-Sn Perovskites, *Small Methods*, 2024, **9**, 2401246, DOI: 10.1002/smtd.202401246.
23 J. M. Ball, *et al.*, Dual-Source Coevaporation of Low-Bandgap $FA_{1-x}Cs_xSn_{1-y}Pb_yI_3$ Perovskites for Photovoltaics, *ACS Energy Lett.*, 2019, **4**, 2748–2756, DOI: 10.1021/acsenergylett.9b01855.
24 A. M. Igual-Muñoz, J. Ávila, P. P. Boix and H. J. Bolink, $FAPb_{0.5}Sn_{0.5}I_3$: A Narrow Bandgap Perovskite Synthesized through Evaporation Methods for Solar Cell Applications, *Sol. RRL*, 2020, **4**, 1900283, DOI: 10.1002/solr.201900283.
25 A. M. Igual-Muñoz, A. Castillo, C. Dreessen, P. P. Boix and H. J. Bolink, Vacuum-Deposited Multication Tin–Lead Perovskite Solar Cells, *ACS Appl. Energy Mater.*, 2020, **3**, 2755–2761, DOI: 10.1021/acsaem.9b02413.
26 K. J. Savill, *et al.*, Impact of Tin Fluoride Additive on the Properties of Mixed Tin-Lead Iodide Perovskite Semiconductors, *Adv. Funct. Mater.*, 2020, **30**, 2005594, DOI: 10.1002/adfm.202005594.
27 Q. Chen, *et al.*, Unveiling Roles of Tin Fluoride Additives in High-Efficiency Low-Bandgap Mixed Tin-Lead Perovskite Solar Cells, *Adv. Energy Mater.*, 2021, **11**, 2101045, DOI: 10.1002/aenm.202101045.
28 J. Nespoli, *et al.*, Quantitative Analysis of the Doping and Defect Density in Mixed Sn–Pb Perovskites Mediated by SnF_2, *Chem. Mater.*, 2025, **37**, 7611–7621, DOI: 10.1021/acs.chemmater.5c00816.
29 H. Yuan, *et al.*, A tin fluoride-free, efficient and durable tin-lead perovskite solar cell, *Nat. Commun.*, 2026, **17**, 360, DOI: 10.1038/s41467-025-65445-0.
30 J. Yan, *et al.*, Crystallization Process for High-Quality $Cs_{0.15}FA_{0.85}PbI_{2.85}Br_{0.15}$ Film Deposited *via* Simplified Sequential Vacuum Evaporation, *ACS Appl. Energy Mater.*, 2023, **6**, 10265–10273, DOI: 10.1021/acsaem.3c00203.
31 Y. Dong, *et al.*, Crystal Growth Modulation of Tin–Lead Halide Perovskites *via* Chaotropic Agent, *J. Am. Chem. Soc.*, 2025, **147**, 31578–31590, DOI: 10.1021/jacs.5c05772.
32 I. Poli, *et al.*, DMSO-Free Processing of Tin–Lead Perovskite Thin Films for Solar Cells with Enhanced Stability, *ACS Energy Lett.*, 2026, **11**, 3416, DOI: 10.1021/acsenergylett.5c03416.
33 C. Li, *et al.*, Diamine chelates for increased stability in mixed Sn–Pb and all-perovskite tandem solar cells, *Nat. Energy*, 2024, **9**, 1388–1396, DOI: 10.1038/s41560-024-01613-8.
34 P. Caprioglio, *et al.*, On the Relation between the Open-Circuit Voltage and Quasi-Fermi Level Splitting in Efficient Perovskite Solar Cells, *Adv. Energy Mater.*, 2019, **9**, 1901631, DOI: 10.1002/aenm.201901631.
35 P. Caprioglio, *et al.*, On the Origin of the Ideality Factor in Perovskite Solar Cells, *Adv. Energy Mater.*, 2020, **10**, 2000502, DOI: 10.1002/aenm.202000502.
36 P. Caprioglio, *et al.*, Open-circuit and short-circuit loss management in wide-gap perovskite p-i-n solar cells, *Nat. Commun.*, 2023, **14**, 932, DOI: 10.1038/s41467-023-36141-8.
37 J. Warby, *et al.*, Understanding Performance Limiting Interfacial Recombination in pin Perovskite Solar Cells, *Adv. Energy Mater.*, 2022, **12**, 21103567, DOI: 10.1002/aenm.202103567.
38 J. Yan, *et al.*, Vacuum Deposited Perovskites with a Controllable Crystal Orientation, *J. Phys. Chem. Lett.*, 2023, **14**, 8787–8795, DOI: 10.1021/acs.jpclett.3c01920.
39 Z. Wang, *et al.*, Frank–van der Merwe-Mediated Sequential Thermal Evaporation for Stable $FASnI_3$ Perovskite Solar Cells, *ACS Nano*, 2025, **20**, 1159–1169, DOI: 10.1021/acsnano.5c16992.
40 M. Ha, *et al.*, Phase Evolution in Methylammonium Tin Halide Perovskites with Variable Temperature Solid-State ^{119}Sn NMR Spectroscopy, *J. Phys. Chem. C*, 2020, **124**, 15015–15027, DOI: 10.1021/acs.jpcc.0c03589.
41 L. Piveteau, V. Morad and M. V. Kovalenko, Solid-State NMR and NQR Spectroscopy of Lead-Halide Perovskite Materials, *J. Am. Chem. Soc.*, 2020, **142**, 19413–19437, DOI: 10.1021/jacs.0c07338.
42 T. J. Jacobsson, *et al.*, Unreacted PbI_2 as a Double-Edged Sword for Enhancing the Performance of Perovskite Solar Cells, *J. Am. Chem. Soc.*, 2016, **138**, 10331–10343, DOI: 10.1021/jacs.6b06320.
43 F. Liu, *et al.*, Is Excess PbI_2 Beneficial for Perovskite Solar Cell Performance?, *Adv. Energy Mater.*, 2016, **6**, 1502206, DOI: 10.1002/aenm.201502206.

44 Y. Gao, H. Raza, Z. Zhang, W. Chen and Z. Liu, Rethinking the Role of Excess/Residual Lead Iodide in Perovskite Solar Cells, *Adv. Funct. Mater.*, 2023, **33**, 2215171, DOI: 10.1002/adfm.202215171.
45 T. J. Savenije, D. Guo, V. M. Caselli and E. M. Hutter, Quantifying Charge Carrier Mobilities and Recombination Rates in Metal Halide Perovskites from Time-Resolved Microwave Photo-conductivity Measurements, *Adv. Energy Mater.*, 2020, **10**, 2000448.
46 Y. Sun, Y. Lai and Y. Yang, Progress of Hole-Transport Layers in Mixed Sn-Pb Perovskite Solar Cells, *Small*, 2024, **20**, 2406991, DOI: 10.1002/smll.202406991.
47 S. Zhumagali, *et al.*, Efficient Narrow Bandgap Pb-Sn Perovskite Solar Cells Through Self-Assembled Hole Transport Layer with Ionic Head, *Adv. Energy Mater.*, 2025, **15**, 2404617, DOI: 10.1002/aenm.202404617.